

# Analysis of jacking forces during pipe jacking in granular materials using particle methods

Xinbo Ji<sup>c</sup>, Pengpeng Ni<sup>a,b,\*</sup>, Marco Barla<sup>d</sup>

<sup>a</sup> School of Civil Engineering, Sun Yat-sen University, Zhuhai 519082, China

<sup>b</sup> School of Civil and Environmental Engineering, Nanyang Technological University, Singapore 639798, Singapore

<sup>c</sup> The Fifth Engineering Co., Ltd. of China, Tiesiju Civil Engineering Group, Jiujiang 332000, China

<sup>d</sup> Department of Structural, Geotechnical and Building Engineering, Politecnico di Torino, Turin, Italy

Received 6 March 2018; accepted 1 March 2019

## Abstract

Trenchless technology is often used in congested urban areas or river crossings to install underground pipelines to minimize disturbance to surface traffic or other activities. Pipe jacking is a typical technique applied to jack pipe segments between two working shafts. However, the design of the jacking force is usually implemented using empirical methods. It should be emphasized that the jacking force will change for each site, depending on the magnitude of overcut, lubricants, work stoppages, geology and misalignment. A particle method is proposed to estimate the jacking force along the pipe. The microparameters are calibrated for sandy soils in Shenyang, so that the macroscale material behavior can be reproduced using the particle model. Hence, the normal force around the pipe circumference can be derived in the particle model, after which the interface friction coefficient is applied to evaluate the friction resistance mobilized at the soil-pipe interface. A modified Protodyakonov's arch model can be used to assess the magnitude of earth pressure acting on the shield face. In the end, the combination of friction resistance and face pressure provides the jacking force. The efficacy of the proposed particle method is demonstrated by comparing calculated jacking forces with those measured in the field for three types of jacking machines in sandy soils under the Hun River, Shenyang.

© 2019 Tongji University and Tongji University Press. Production and hosting by Elsevier B.V. on behalf of Owner. This is an open access article under the CC BY-NC-ND license (<http://creativecommons.org/licenses/by-nc-nd/4.0/>).

**Keywords:** Pipe jacking; Jacking force; Particle methods; Distinct element

## 1 Introduction

Pipe jacking is a type of trenchless technology for installing underground infrastructure, such as sewers, pressurized pipelines (oil, gas and water), and electricity and communication lines (Najafi, 2005). A launch shaft is excavated, allowing the setup of the jacking systems, including the guide frame, the thrust wall and the main jacking station. A receiving shaft is excavated as a target for the shield machine, behind which pipe segments are pushed into

place. A pipe jacking project requires minimum ground excavation and causes less disruption to surface traffic and other human activities, which is an advantage for use in congested urban areas compared to the conventional open-and-cut method. In river crossings, traditional approaches are hard to implement, whereas the pipe jacking technique can be easily employed.

Pipe jacking has been used extensively in different geological formations worldwide. For example, Barla, Camusso, and Aiassa (2006) presented a case study of jacking a vitrified clay pipe with a diameter of 600 mm under a main road with heavy traffic at Martina Franca, Italy. The pipe jacking project passed through the Altamura limestone

\* Corresponding author at: School of Civil Engineering, Sun Yat-sen University, Zhuhai 519082, China.

E-mail address: [pengpeng.ni@ntu.edu.sg](mailto:pengpeng.ni@ntu.edu.sg) (P. Ni).

<https://doi.org/10.1016/j.undsp.2019.03.002>

2467-9674/© 2019 Tongji University and Tongji University Press. Production and hosting by Elsevier B.V. on behalf of Owner. This is an open access article under the CC BY-NC-ND license (<http://creativecommons.org/licenses/by-nc-nd/4.0/>).

with local inclusions of micrite, with a great challenge in the presence of a horizontal bedding plane. Cui, Xu, Shen, Yin, and Horpibulsuk (2015) reported the field performance of concrete pipes during jacking in cemented sand silt across the Guan River in Xiangshui, China. Cheng, Ni, Shen, and Huang (2017) summarized four cases of slurry pipe jacking in the Shulin district sewer network in Taipei and indicated that the jacking force could be influenced by overcut, lubricants, work stoppages, geology and misalignment. The technique has also been used for challenging projects such as a large-section long pedestrian underpass (width of 7 m, height of 4.3 m, and jacking distance of 94.5 m) in muddy silty clay in Nanjing, China (Zhang, Liu, & Qin, 2016), a curved pipe jacking roof (transition curve of 88 m and circular curve of 167 m) for the Gongbei Tunnel in Zhuhai, China (Zhang, Ma et al., 2016), and a large long concrete pipe jacking project (3.5 m in diameter and 1 000 m in length) in sandy soils through the Hun River in Shenyang, China (Ji et al., 2017).

Different methods have been proposed to evaluate the jacking force, which is of essential importance for pipe jacking projects as the estimation of project completion time and costs are all correlated. Chapman and Ichioka (1999) compiled a database containing 236 projects using slurry shield machines, 113 projects using auger machines, and 49 projects using push-in machines, based on which three empirical methods were developed. Most present empirical approaches do not distinguish the effects of face pressure, shield friction, pipe friction and edge resistance. For pipe jacking, earth pressures acting on the shield excavation face were often calculated using different forms of arching models (Ji, Ni, Barla, Zhao, & Mei, 2018; Zhang, Zhang, Zhou, Dong, & Ma, 2016).

As pipe segments are jacked through different geological formations with a significant variation in the pipe alignment, the calculation of friction mobilized at the soil-pipe interface becomes critical in the estimation of the jacking force. Milligan and Norris (1999) initially conducted a series of interface tests to determine the conceptual models for soil-pipe interaction, taking into account the effect of localized ‘asperities’. The friction coefficient at the soil-pipe interface is often assumed to be a fraction of the soil friction angle. Pellet-Beaucour and Kastner (2002) suggested the use of a conservative range of interface friction over the soil friction ratio between 1/2 and 1. The interface friction could also be affected by the shape of the cross section of the pipe (Shimada, Khazaei, & Matsui, 2004). Barla et al. (2006) used the product of the weight of the pipe and the interface friction coefficient to evaluate the friction force. However, the normal forces acting around the pipe circumference should be calculated. The effect of a ‘wavy’ shaped pipe alignment on the interface friction should also be considered, since the ‘wavy’ shaped pipe alignment will increase the friction forces significantly (Broere, Faassen, Arends, & van Tol, 2007; Milligan & Norris, 1999; Shou & Jiang, 2010). The importance of introducing lubricants to reduce the interface friction has been discussed and

demonstrated by researchers using numerical simulations (Shou, Yen, & Liu, 2010) and laboratory experiments (Namli & Guler, 2017; Reilly & Orr, 2017).

Numerical modeling can be used to evaluate the interface friction by explicitly considering the normal forces acting around the pipe circumference and the effect of pipe misalignment. For example, Li, Emeriault, Kastner, and Zhang (2009) analyzed the face stability of large slurry shield-driven tunnels in a three-dimensional finite difference program. Yen and Shou (2015) conducted simulations using a three-dimensional finite element software for the estimation of the jacking force for a pipe jacking project. However, these approaches cannot properly model the interaction between soil particles and the pipe, and the calculation is often very time-consuming. Alternatively, researchers used the distinct element method to characterize the soil behavior, where the discontinuity in the rock mass (Huang & Zhang, 2012), the cementation bonding between soil particles (Barla & Camusso, 2013; Camusso & Barla, 2009), the influence of tail gaps (Jiang & Yin, 2012), and the effect of soil conditioning (Jiang & Yin, 2014) can be simulated. Ji, Zhao et al. (2019) proposed a method to estimate the jacking force for pipe jacking in sandy soils, where the effects of face pressure, frictions mobilized at the soil-pipe interface, and pipe alignment were explicitly considered.

In this investigation, a distinct element model is proposed to simulate the behavior of sandy soils in Shenyang, China. The maximum and minimum values of porosity are calculated using different packing methods for spherical elements, representing the soil particles. The calibration process of the numerical model is presented by comparing simulated shear strengths with those measured in consolidated drained triaxial tests, where the determination of microparameters is explicitly explained. A parametric study was conducted to investigate the influence of rate of loading, confining stress, and specimen dimensions on the stress strain curve of soil. In the end, a field case is given to show how the distinct element model of Ji, Zhao et al. (2019) can be used to calculate the jacking force for a pipe jacking project in sandy soils.

## 2 Generation of the synthetic specimen

### 2.1 Properties of sandy soils

In Shenyang, China, the elevation of the northeast part is higher than the elevation of the southwest part, with an average of the ground surface at 45 m. The thickness of the aquifer varies between 18 m and 30 m, below which a soil layer mixed with silty clay and boulder clay can be regarded as an impermeable layer. In the zone of the aquifer, sandy soils are dominant, mixing with a small fraction of silty clay. For pipe jacking, the burial depth is often selected to be greater than 2.5 times the pipe diameter (Najafi, 2005). Hence, for the most part, pipe segments need to be jacked through sandy soils in Shenyang. Three

typical sandy soils were taken from different sites in Shenyang, as illustrated in Fig. 1. For each group, sieve analysis was conducted 10 times, and the average particle size distribution curves are plotted in Fig. 2. Table 1 summarizes all physical properties measured for these three sandy soils.

## 2.2 Particle size distribution

In this investigation, the commercially available distinct element code, PFC<sup>2D</sup>, is employed to simulate the macroscale material behavior using microscale components. Spherical elements are used to represent a clump of several soil particles. The micromechanical parameters need to be calibrated, so that the assembly of clumps can reproduce the macroscale mechanical response of sandy soils. The interaction between clumps and the strength of the spherical element itself determines the behavior of the synthetic material.

As an initial step, the particle size distribution of spherical elements should be defined. As an interpretation of Fig. 2, one can infer that the particle size distribution curves spread widely for sandy soils at different sites. In reality, soil particles cover a wide range from 0.01 mm to 100 mm. However, it is impractical to model the synthetic material using the real particle sizes, which will result in an enormous number of spherical elements and slow down the analysis significantly. A unified particle size distribution curve should, therefore, be defined to represent the behavior of all sandy soils for ease of modeling. In this study, the restrained particle size distributes from 5 mm to 20 mm, so that the influence of extremely fine and coarse particles is ignored. The mechanical response of granular material is heavily dependent on its grain size distribution (Liu et al., 2014; Yin, Hicher, Dano, & Jin, 2017; Yin, Huang, & Hicher, 2016; Yin, Zhao, & Hicher, 2014). Although the size for all particles is limited to a narrow range, causing different grain size distribution as illustrated in Fig. 2 compared to the reality, the proportion of particles in different sizes is carefully controlled to reproduce the grading-dependent macromechanical behavior for real sands. Following the study of Camusso and Barla (2009), the percentage of passing for a specific particle size can be calculated in the range of 5–20 mm as follows:

$$P'_x = P_x - P_5 \cdot \frac{\lg 20 - \lg x}{\lg 20 - \lg 5}, \quad (1)$$



Fig. 1. Three types of sandy soils in Shenyang: (a) sand 1, (b) sand 2, and (c) sand 3.

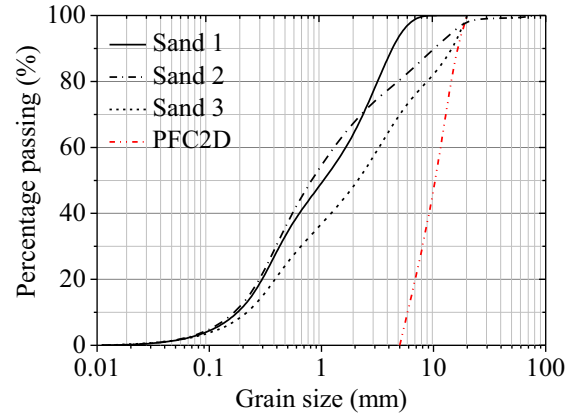


Fig. 2. Particle size distribution curves for sandy soils in the field and in the numerical model.

where  $P_x$  represents the percentage of passing of the real sandy soil,  $P'_x$  corresponds to the modified percentage,  $x$  shows the generic dimension of spherical elements.

The comparison between measured and modified particle size distribution curves is depicted in Fig. 2. The modified particle size distribution curve is then divided into 3 intervals with an equal width of 5 mm. The number of spherical elements in each interval is defined as  $N_i$  by:

$$N_i = \frac{V_{s,i}}{A_{avg,i}}, \quad (2)$$

where  $V_{s,i}$  denotes the volume, and  $A_{avg,i}$  is the average area of spherical elements pertaining to the  $i$ -th interval. Based on the modified particle size distribution curve, the total volume of spherical elements  $V_{s,i}$  can be determined from the specimen volume and the material porosity. The average area  $A_{avg,i}$  can be evaluated by the following expression:

$$A_{avg,i} = \pi \cdot \frac{r_{max,i}^3 - r_{min,i}^3}{3(r_{max,i} - r_{min,i})}, \quad (3)$$

in which  $r_{max,i}$  and  $r_{min,i}$  represent the maximum and minimum radii of the spherical elements in the  $i$ -th interval, respectively.

## 2.3 Two-dimensional porosity

In this investigation, the mechanical behavior of a two-dimensional synthetic material is simulated using particle methods. The efficacy of the numerical model is assessed by comparing the calculated soil shear strengths under the plane strain biaxial compression conditions with the soil shear strengths measured under the consolidated drained triaxial compression conditions. Although the shear strength under the plane strain conditions could be slightly different from the shear strength obtained under the triaxial compression conditions, the two-dimensional model is calibrated for ease of analysis of the normal force acting around the pipe circumference during pipe jacking.

Table 1  
Physical properties of sandy soils.

Soil	Water content (%)	Specific gravity	Dry density (g/cm <sup>3</sup> )	Minimum dry density (g/cm <sup>3</sup> )	Maximum dry density (g/cm <sup>3</sup> )
Sand 1	11.1	2.66	1.531	1.37	1.65
Sand 2	28.5	2.63	1.582	1.35	1.75
Sand 3	21.0	2.62	1.723	1.55	2.09

The two-dimensional porosity needs to be determined by the synthetic material. In PFC<sup>2D</sup>, the porosity is calculated as the ratio between voids and the total area of a measurement circle. Camusso and Barla (2009) stated that the two-dimensional porosity could be lower than the corresponding three-dimensional value. For an ideal case with uniform spherical elements as shown in Fig. 3, the maximum and minimum densities can be achieved by packing all elements in the hexagonal and cubic states, respectively, and the corresponding minimum and maximum porosities are  $n_{min} = 9.31\%$  and  $n_{max} = 21.64\%$ . The two-dimensional porosity ( $n_{2D}$ ) can be correlated with the relative density  $D_r$ , the minimum and maximum void ratios (i.e.,  $e_{min,2D}$  and  $e_{max,2D}$ ) as follows:

$$e_{2D} = e_{max,2D} - D_r(e_{max,2D} - e_{min,2D}), \quad (4)$$

$$n_{2D} = \frac{e_{2D}}{1 + e_{2D}}. \quad (5)$$

The packing method for spherical elements will influence the calculated porosity, which is critical to reproduce the macroscale material behavior using microscale components. A pluviation technique is proposed as schematically shown in Fig. 4 to produce the minimum packing state conforming to the ASTM D 4254 standard. The density of particle materials has long been estimated to increase with the kinetic energy of dropped particles, which is also positively correlated with the failing height. Hence, a low-density state can be achieved using the air pluviation technique when a small failing height is employed. The opening with a size of 0.05 m is then assigned at a distance of 0.1 m from the base. Once a layer of particles has fallen in position, the opening moves vertically by 0.1 m. The opening follows a S-shaped pattern starting from the left bottom corner. After the desired height of the specimen is reached, three

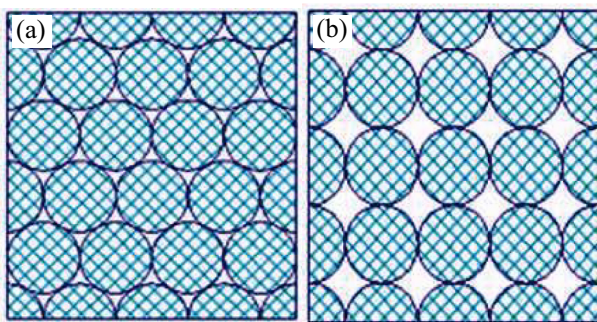


Fig. 3. Correlation of two-dimensional porosity with the compaction condition of sands: (a) maximum density with  $n = 9.31\%$ , and (b) minimum density with  $n = 21.64\%$ .

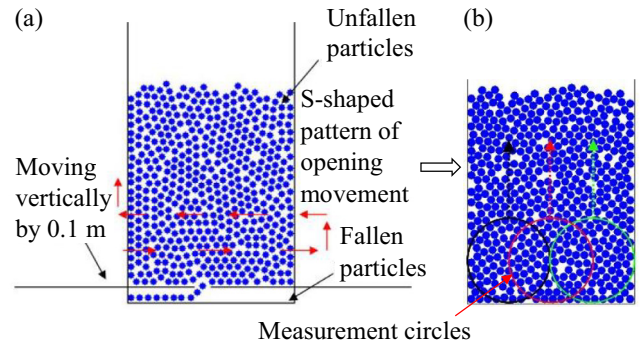


Fig. 4. Minimum packing using pluviation methods: (a) illustration of opening movement, and (b) measurement circles for density calculation.

measurement circles with a radius of 0.25 m are used to monitor the variation in density along the height. The porosity ( $n$ ) measured using the measurement circle method in PFC<sup>2D</sup> can be computed by

$$n = \frac{A^{void}}{A^{circle}} = \frac{A^{circle} - A^{ball}}{A^{circle}} = 1 - \frac{A^{ball}}{A^{circle}}, \quad (6)$$

$$A^{ball} = \sum_{N_p} (A^P - A^{overlap}), \quad (7)$$

where  $A^{circle}$  is the area of the measurement circle,  $A^{void}$  shows the area of voids, and  $A^{ball}$  denotes the area of spherical elements. During the packing process of the spherical elements, overlapping of particles could occur. Therefore, the number of particles within a measurement circle should be counted as  $N_p$ , and the difference in the area of particles with and without considering overlapping (i.e.,  $A^P$  and  $A^{overlap}$ ) can then be evaluated to determine the value of  $A^{ball}$ .

The total volume of the specimen is defined as 0.5 m<sup>2</sup>, and 500 spherical elements are allowed to fill the container between three fixed walls (one bottom and two lateral walls). The radius of particles is selected as 12.5 mm, and the density is 2 g/cm<sup>3</sup>, which is on the upper bound of density for three sandy soils. At this stage, microparameters have not been calibrated. A set of microparameters is used to simulate the stiffness of particles (normal and tangential stiffnesses of  $k_n = k_s = 10^8$  N/m) and the interaction between particles (friction coefficient of  $\mu = 1$ ).

Following the ASTM D 4253 standard, sand samples should be placed on a vibratory table to achieve the maximum packing state. Two separate approaches are proposed in this investigation for spherical elements as presented in Fig. 5: vibration only in the vertical direction, and vibration in both the horizontal and vertical directions. An

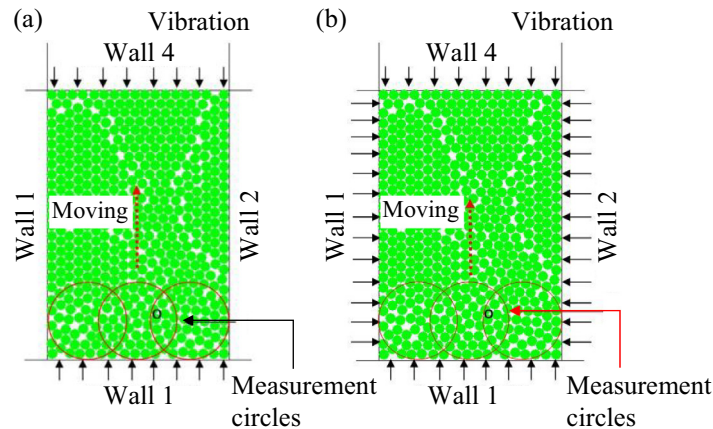


Fig. 5. Maximum packing using vibration methods: (a) vibration in the vertical direction, and (b) vibration in both the horizontal and vertical directions.

overload of 14 kPa is applied to the boundaries of the specimen, where a displacement-controlled vibration is excited with a frequency of 60 Hz and an amplitude of 0.165 mm. As vibration continues, all spherical elements will be compacted to a denser state, and the maximum density is dependent on the geometries of the particles. The loading error is calculated by comparing the stress at the wall and the applied stress. Vibration is terminated once the loading error is less than a predefined criterion (i.e., 0.05%). During the vibration stage, the friction coefficient between particles is set to 0, and the stiffnesses of particles are reduced by 1/10 to minimize the computational time. Again, measurement circles with a radius of 0.3 m are used to monitor the uniformity along the height. The size of the specimen in maximum density tests is greater than the size of the specimen in minimum density tests for ease of vibration control.

#### 2.4 Evaluation of the numerical model for porosity calculations

Different factors can influence the accuracy of porosity calculations, and the results are shown in Fig. 6. One parameter varies in the parametric study, and all other parameters are kept constant as defined previously. For the maximum porosity case, the impact of the friction coefficient between particles ( $\mu$ ), falling height and density of particles ( $\rho$ ) are systematically investigated. The interparticle friction has a significant influence on the calculation of two-dimensional porosity. When the  $\mu$  value increases from 0 (perfectly smooth) to 0.5, the porosity is doubled. However, when the interparticle friction exists, the variation of  $\mu$  does not lead to a huge difference in the estimations of porosity. When the opening is set at a lower height, the porosity is expected to be higher, approaching the theoretical maximum porosity. For a higher failing height, the kinetic energy is anticipated to be greater, resulting in a state that is more densely compacted with a lower porosity. The influence of the density of particles is insignificant, probably because of the low value of the failing height used

in the analysis. For the minimum porosity case, the sensitivity of porosity to the mode, amplitude ( $A$ ) and frequency of vibration is studied. The advantage of applying vibration in both the horizontal and vertical directions is apparent compared to the vertical mode of vibration, since the calculated porosity is closer to the theoretical minimum value. When the amplitude of the vibration changes from 0.1 mm to 1 mm, the porosity decreases initially to the minimum value at  $A = 0.2$  mm, after which the calculated porosity becomes larger. The amplitude of the vibration should be selected as  $A = 0.2$  mm to obtain the optimal maximum compaction. The influence of vibration frequency is also investigated, and the results of porosity seem to be smallest when the frequency varies between 60 Hz and 90 Hz.

The number of particles in each interval can be calculated using Eqs. (2) and (3). Based on the parametric study, the optimal performance of packing methods is determined by using an opening size of 40 mm (i.e., 2 times the maximum particle size) and the biaxial vibration mode with an amplitude of 0.2 mm and a frequency of 60 Hz for the loosest and densest compacted conditions, respectively. The comparison of porosity between theoretical and numerical solutions is presented in Fig. 7. In the numerical model, the average maximum and minimum values of porosity are derived as 0.2 and 0.124, respectively. These extreme limits of porosity are substituted into Eq. (5), from which the maximum and minimum void ratio can be evaluated. Assuming that the relative density of typical sandy soils in Shenyang is 70%, Eq. (4) can provide the two-dimensional porosity ( $n_{2D}$ ) for use in Eq. (5), and the void ratio for the modified particle size distribution is determined as 14.8%.

### 3 Biaxial compression tests

#### 3.1 Calibration of microparameters

The synthetic specimen contains an assembly of spherical elements following the modified particle size

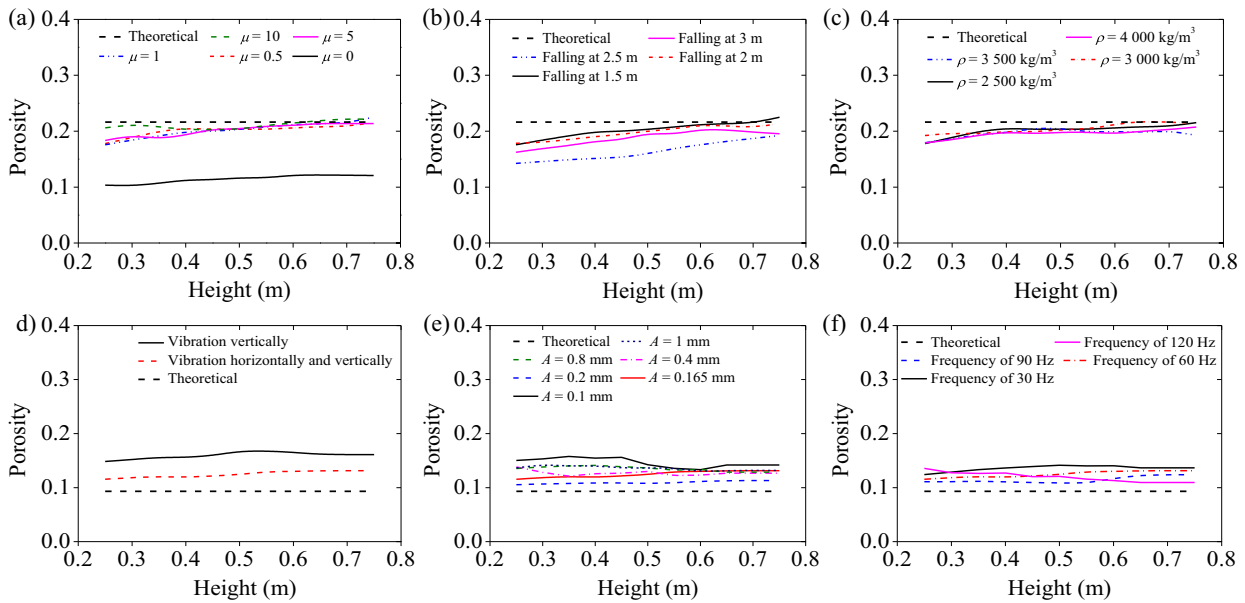


Fig. 6. Calibration of numerical model for two-dimensional porosity: (a) effect of friction coefficient between particles on maximum porosity, (b) effect of falling height on maximum porosity, (c) effect of particle density on maximum porosity, (d) effect of vibration direction on minimum porosity, (e) effect of vibration amplitude on minimum porosity, and (f) effect of vibration frequency on minimum porosity.

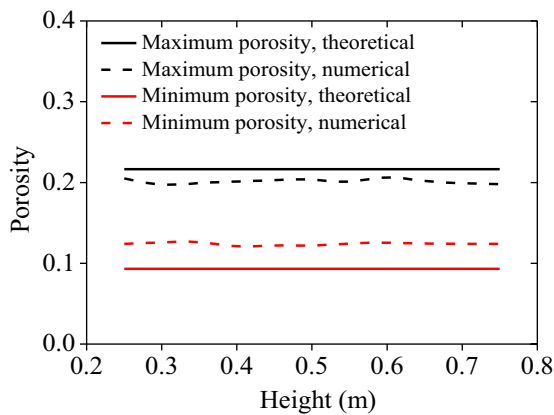


Fig. 7. Comparison of porosity between theoretical and numerical solutions.

distribution and the calculated porosity within smooth rigid walls. During the generation process, particles may have initial overlap, at which excessive particle velocity and stress concentration could occur. Hence, the diameters of particles are increased gradually in 9 steps to reach their final sizes to avoid particle overlap. All particles are generated within boundaries, and the iteration is stopped until the nonuniform stresses within particles are balanced for each step. In addition, a measurement circle with a radius of 0.15 m is set at the center of the specimen. For each iteration, the difference between calculated and theoretical porosities should be less than 5% (i.e.,  $n_{2D} = 0.141-0.155$ ). Interested readers can find more details of the expansion law for particle size in Camusso and Barla (2009).

The efficacy of the numerical model is evaluated by comparing calculated strength parameters under the biaxial

compression conditions with those measured in consolidated drained triaxial compression tests. The soil specimen in triaxial tests has dimensions of 0.3 m in diameter and 0.6 m in height. Therefore, the numerical model under the plane strain conditions should have a width of 0.3 m and a height of 0.6 m. All particles are divided into three intervals, and the number of particles in each interval for the modified particle size distribution is listed in Table 2. The expansion law for particle size is summarized in Table 3. In the end, a specimen is generated following the modified particle size distribution with a porosity of 0.145.

All particles are rigid, with an initial elastic modulus of  $E_c = 50$  MPa. The stiffnesses between particles and the interparticle friction coefficient are set as  $k_n = k_s = 10^8$  N/m and  $\mu = 1$ , respectively, during the consolidation stage. Four smooth rigid walls are controlled to apply a confining stress of  $\sigma_x = \sigma_y = 200$  kPa to allow the specimen to fully consolidate. The stresses within the specimen are measured using measurement circles, and the consolidation stage is terminated until the measured stresses are very close to the applied confining pressure (i.e., error less than 0.05%). The loading rate could significantly influence the results of the laboratory element tests for the soils. Ni, Mei, Zhao, and Chen (2018) conducted plane strain tests on reconstructed silty clay using a loading rate varying between 0.001 92 mm/min and 4 mm /min. Ni (2016)

Table 2  
Number of particles in different intervals for the modified particle size distribution.

Interval of particle size (mm)	5–10	10–15	15–20
Number of particles	1 446	539	82

Table 3  
Scale factor for radius of particles.

Step	1	2	3	4	5	6	7	8	9
Scale factor	2	1.49	1.26	1.13	1.07	1.03	1.01	1.005	1

performed consolidated drained triaxial compression tests on Synthetic Olivine sand using at loading rate of 1 mm/min. The current numerical simulation follows the triaxial tests of Ji (2017) on sandy soils in Shenyang, where a loading rate of 0.6 mm/min was applied on top of the specimen.

The shear strength measured in plane strain tests is well known to differ slightly from the shear strength measured in triaxial compression tests. During loading, the stiffnesses between particles and the interparticle friction coefficient are readjusted. The macroscale material behavior calculated from triaxial tests and biaxial simulations is compared in Table 4. The internal friction angle is determined by constructing Mohr circles at different confining stresses. The deformation modulus measured at 50% of the peak shear strength is defined as  $E_{50}$ . These two macroscale material parameters measured in triaxial tests can well be reproduced by biaxial numerical simulations using microparameters of  $k_n = k_s = 2 \times 10^8$  N/m and  $\mu = 2$ . The modeling strategy of reducing the particle size in a narrow range rather than using the real particle size distribution is demonstrated to be effective and is also much less expensive computationally.

### 3.2 Parametric study

A parametric study is carried out to investigate how the rate of loading, confining stress, and specimen dimensions can affect the calculation of shear strength parameters. Assuming that the target loading rate is 0.01 mm/s (i.e., 0.6 mm/min), four loading patterns are defined as shown in Fig. 8 and Table 5. For each loading pattern, the target loading rate is reached after 10 000 steps of iteration. The results of the stress strain curves at a confining stress of 200 kPa calculated for these four loading patterns are illustrated in Fig. 9. The peak shear strength is generally consis-

Table 4  
Comparison of macroscale material behavior between triaxial tests and biaxial simulations.

Test	Confining stress (kPa)	$E_{50}$ (MPa)	Friction angle ( $^\circ$ )
Triaxial tests	100	68.15	38.0
	150	70.10	38.0
	200	71.20	38.0
	250	73.00	38.0
	400	74.80	38.0
Biaxial simulations	100	62.60	37.4
	150	69.10	37.4
	200	70.00	37.4
	250	72.00	37.4
	400	76.00	37.4

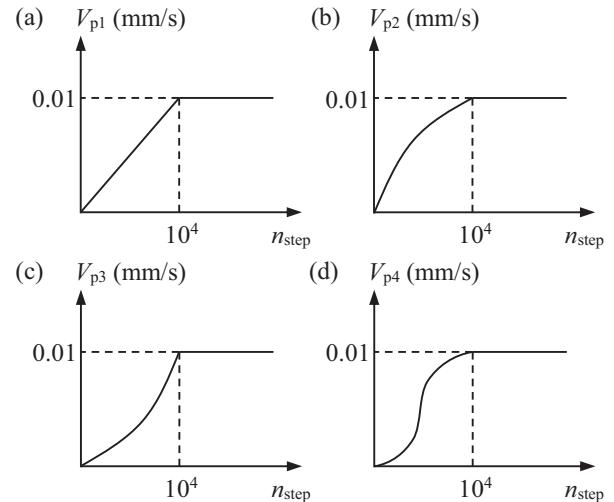


Fig. 8. Different loading patterns: (a) constant rate of loading, (b) decreased rate of loading, (c) increased rate of loading, and (d) varying rate of loading.

tent for different cases. However, the loading rate can change the brittleness of the specimen, where the strain corresponding to the peak strength varies with the loading pattern. The case with constant rate of loading is suggested for ease of implementation.

Figure 10 presents the influence of the confining stress on the calculated stress strain curves. As expected, with the increase of confining stress, the peak strength becomes higher, and the strain corresponding to the peak strength is larger. The whole stress strain curve moves upwards with the confining stress. However, at high confining stress, the phenomenon of strain softening becomes more apparent.

The width ( $W$ ) of the specimen is fixed at 0.3 m, and the height ( $H$ ) of the specimen varies from 0.3 m, 0.6 m to 1.2 m to represent three cases with different ratios of height over width. The influence of the height over width ratio for specimens on the stress strain curves is demonstrated in Fig. 11. For a smaller height over width ratio of 1, the stress strain curve presents the strain softening stage more dramatically. When the height over width ratio varies between 2 and 4, the stress strain curves do not show significant difference. In general, for a larger height over width ratio, the specimen is less influenced by the loading pattern at both ends, and the strain at the peak strength decreases because the constraints at both ends are less significant for a more slender specimen, where free development of stress along the specimen is allowed to decrease the peak strength and the associated strain (Wang, Huang, Ni, Ranjith, & Zhang, 2013). With the increase in the confining stress,

Table 5  
Mathematical forms of four loading patterns.

Pattern	Loading (mm/s)	Rate of loading (mm <sup>2</sup> /s)	Target (mm/s)
Constant	$V_{p1} = A_d \cdot (n_{step} \cdot t_s)$	$a_{p1} = A_d \cdot t_s$	0.01
Decreased	$V_{p2} = A_c \cdot (n_{step} \cdot t_s)^{0.5}$	$a_{p2} = 0.5 \cdot A_c \cdot t_s \cdot (n_{step} \cdot t_s)^{-0.5}$	0.01
Increased	$V_{p3} = A_b \cdot (n_{step} \cdot t_s)^2$	$a_{p3} = 2 \cdot A_b \cdot t_s \cdot (n_{step} \cdot t_s)$	0.01
Varying	$V_{p4} = A_a \cdot (n_{step} \cdot t_s - \cos((n_{step,tot} \cdot t_s)^{-1} \cdot 2\pi - \frac{\pi}{2}) / n_{step} \cdot t_s \omega_a)$	$a_{p4} = A_a \cdot (1 + \sin((n_{step,tot} \cdot t_s)^{-1} \cdot 2\pi \cdot t_s - \frac{\pi}{2}))$	0.01

Note:  $V_p$  is the target loading,  $t_s$  denotes the computational time for each iteration,  $A_a$  represents the amplitude of rate of loading,  $A_b$ ,  $A_c$  and  $A_d$  are constants,  $n_{step}$  is the total number of iterations during the whole loading process, and  $n_{step,tot}$  corresponds to the total number of iterations before reaching the target loading, and  $\omega_a = (n_{step,tot} \cdot t_s)^{-1} \cdot 2\pi$ .

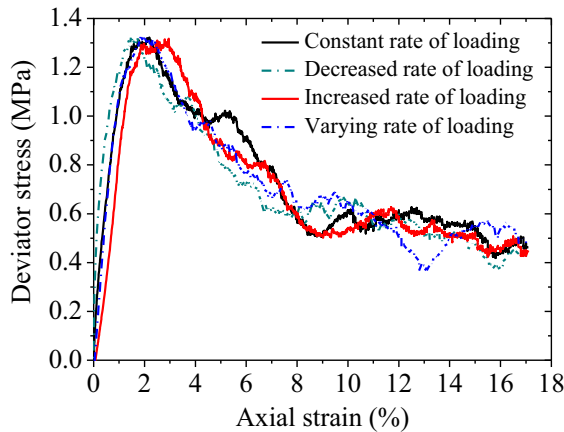


Fig. 9. Influence of rate of loading on the stress strain curve.

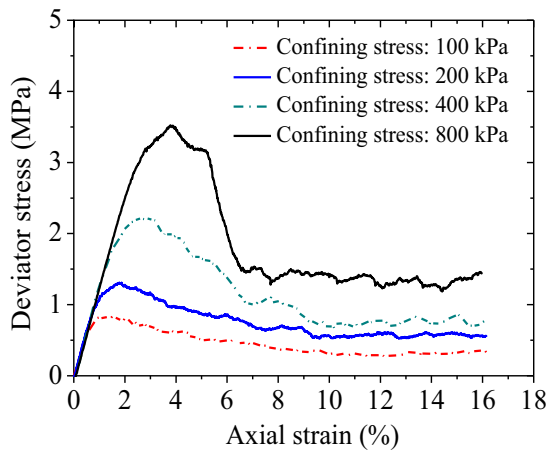


Fig. 10. Influence of confining stress on the stress strain curve.

the peak strength is increased, and the influence of the end effect becomes less obvious.

The impact of specimen size is investigated using three specimens with equal height and width at 0.3 m, 0.6 m, and 0.9 m. Figure 12 shows the calculated stress strain curves for three specimen sizes. When the height over width ratio is fixed, the specimen size does not result in significant difference in the calculated strength and the pattern of stress strain curves. In general, a higher confining stress corresponds to a larger peak strength, and the associated strain also increases, consistent with the observations in

the uniaxial compression tests on rocks (Wang et al., 2013) that the size effect is not apparent, but the behavior of specimens is mostly affected by the end effect.

## 4 Calculation of jack force

### 4.1 Field case

The Wu'ai Electrical Power Tunnel was constructed to cross the Hun River in Shenyang, China, where the trenchless technology of pipe jacking is used to jack a 3.5 m diameter reinforced concrete pipe through 1 000 m. The pipe jacking project contains three phases. As illustrated in Fig. 13, a hand shield machine is used first to jack the pipe from the #2 shaft to the #3 shaft in a length of 170 m. The #3 shaft serves as the receiving shaft for the hand shield jacking but also acts as the launch shaft for the pipe jacking to the #4 shaft on the other side of the Hun River. This second phase jacking is implemented using an earth pressure balance (EPB) machine. However, the second jacking project fails after a 160 m drive, and more details about the incident can be found in Ji et al. (2017). An alternative route is therefore sought near the second phase of jacking, where a slurry shield (SS) machine is used to jack the pipe from the #5 launch shaft to the #4 receiving shaft in a length of 830 m. The first phase of jacking is downslope, with an angle of  $-1.42\%$ . The second and third phases of jacking follow a downslope angle of  $-1.42\%$  initially, and the slope changes to  $-0.3\%$  after approximately 1/3 of the jacking distance.

The reinforced concrete pipe segment is made to have an inside diameter of 3.5 m, a wall thickness of 0.32 m, and a length of 2.5 m. The pipe is buried at a depth of approximately 9 m. At the site, the typical sandy soil in Shenyang is encountered, mixed with round gravel and silty clay. More details about the project and the geological information of the site can be found in Ji et al. (2017).

### 4.2 Distinct element modeling

The jacking force contains two primary components: the earth pressure acting on the shield face and the friction mobilized at the soil-pipe interface. In this investigation, the earth pressure acting on the shield face is estimated using the analytical method of Ji, Ni et al. (2019) based



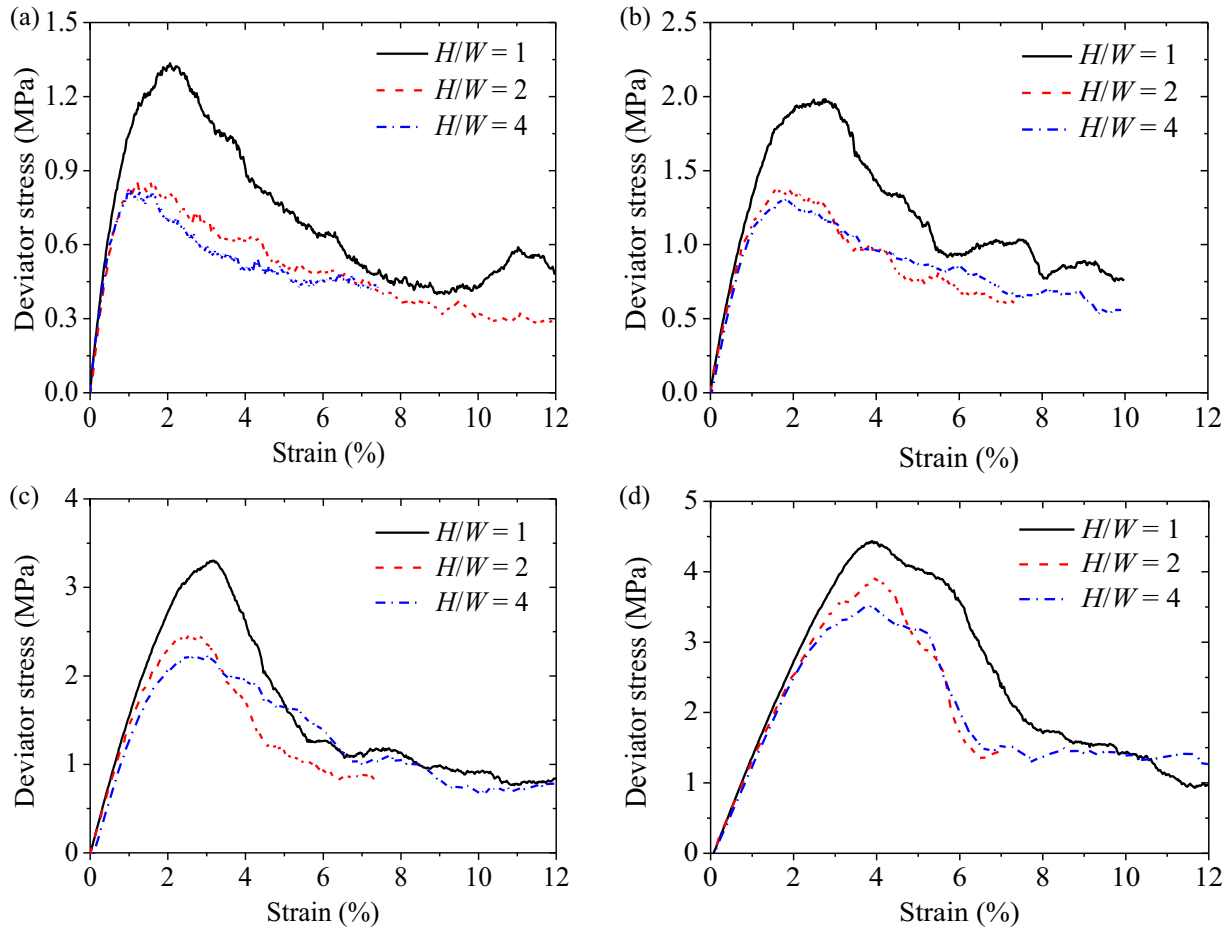


Fig. 11. Influence of height over width ratio of specimens on the stress strain curve: (a) confining stress of 100 kPa, (b) confining stress of 200 kPa, (c) confining stress of 400 kPa, and (d) confining stress of 800 kPa.

on the modified Protodyakonov's arch model. The friction between soil and pipe is calculated as the product of the normal force acting around the pipe circumference and the interface friction coefficient. A series of interface tests has been conducted by Ji (2017) to assess the variations of interface friction with the surrounding soil and slurry lubricants. Ji, Zhao et al. (2019) presented a design table, where the friction coefficient at the interface between different pipe and soil materials can be interpreted. Hence, the interface friction is not explicitly modeled in the distinct element analysis, and the influence of interface friction is considered to reduce the normal force acting on the pipe.

Following the study of Ji, Zhao et al. (2019), it is not necessary to model the entire pipe jacking process in three dimensions, which could be computationally expensive. Instead, two-dimensional modeling under the plane strain conditions was conducted. The normal force acting around the pipe circumference is calculated section by section along the jacking distance using the calibrated distinct element model under the plane strain conditions. The soil medium is modeled to have a width of more than 5 times larger than the pipe diameter to eliminate the boundary effects (Ni, Moore, & Take, 2018; Ni, Qin, & Yi, 2018). The pipe is excavated to have a diameter of 3.5 m, and

an overcut of 50 mm is also implemented. The synthetic material is generated following the modified particle size distribution and the calculated porosity. All spherical elements are solid, but overlapping between particles is allowed to model the deformability characteristics of geomaterials. Clumps with 3 random spherical elements are implemented to replace some particles, so that the effect of particle angularity can be simulated. All microparameters are defined as  $E_c = 50$  MPa,  $k_n = k_s = 2 \times 10^8$  N/m and  $\mu = 2$ .

The lining is assumed to have a unit weight of  $25$  kN/m<sup>3</sup>, and a thickness of 0.1 m. Two types of lining models were developed to simulate the interaction between the pipe and the soil-slurry mixture. One approach is to simplify the lining using a single big particle as illustrated in Fig. 14(a) with a diameter of 3.5 m. Since the size of the lining is increased, the unit weight of the big particle is decreased to  $9$  kN/m<sup>3</sup> to reproduce the equivalent stress level. Another technique is to simulate the lining with the exact thickness using a layer of bonded small particles as presented in Fig. 14(b). Parameters for the parallel bond model between lining particles are defined as: parallel bond radius multiplier of 3, and both normal and shear strengths of  $10^{15}$  Pa/m. The two modeling strategies for lining can

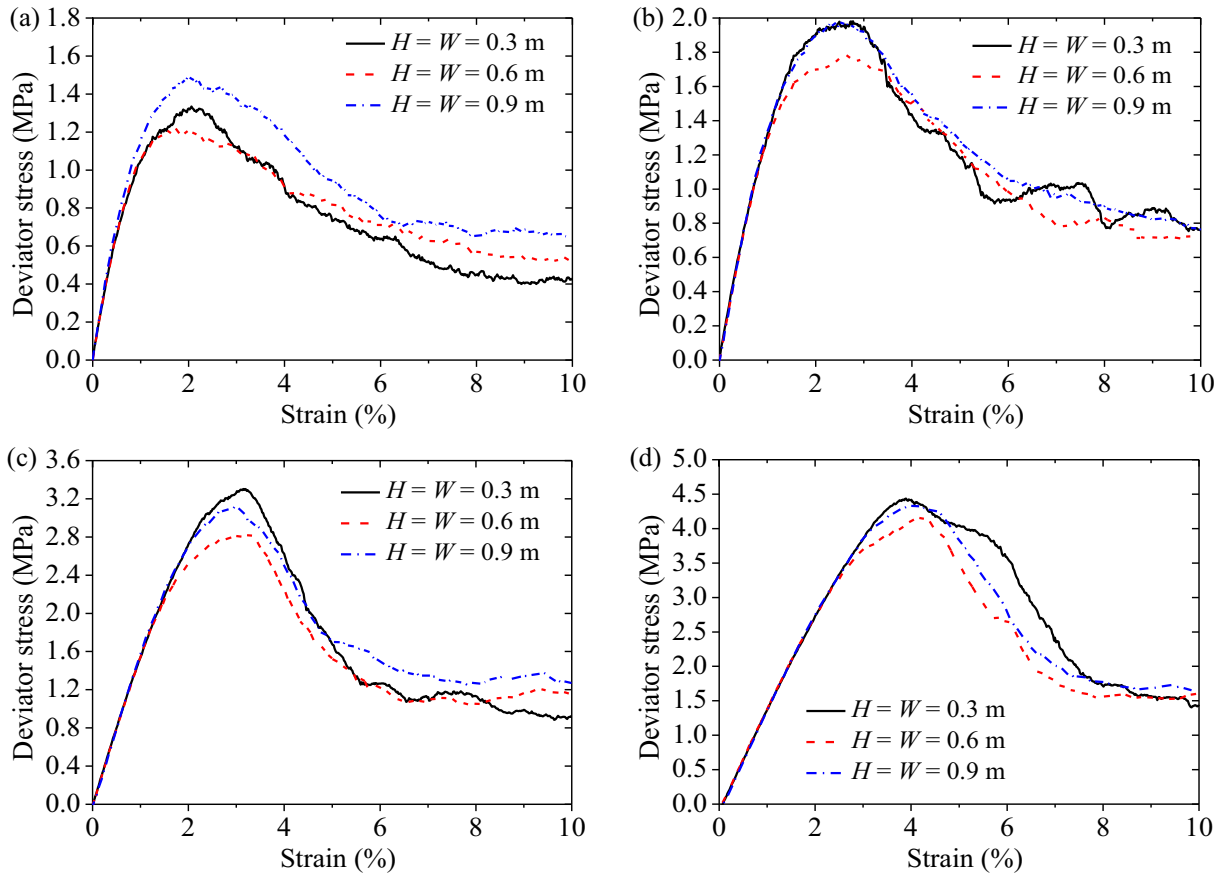


Fig. 12. Influence of specimen size on the stress strain curve: (a) confining stress of 100 kPa, (b) confining stress of 200 kPa, (c) confining stress of 400 kPa, and (d) confining stress of 800 kPa.

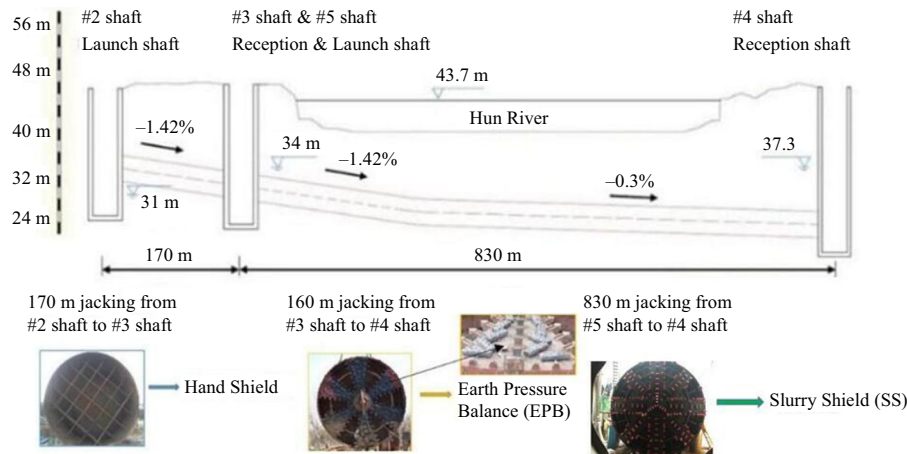


Fig. 13. Elevation view of the pipe jacking project of Wu'ai Electric Power Tunnel.

produce similar results, and interested readers are directed to Ji (2017) and Ji, Zhao et al. (2019) for more details.

Once the friction mobilized at the soil-pipe interface at different section is obtained, the angular deviation influence factor can be incorporated based on the variation of pipe alignment. Ji, Zhao et al. (2019) presented a design table for use to estimate the angular deviation influence factor, which can reach up to 1.05 when the pipe misalignment

is  $2^\circ$ . More details of the distinct element method can be found in Ji, Zhao et al. (2019).

#### 4.3 Comparison between calculated and measured jacking forces

The jacking forces as a function of jacking distance are calculated using the proposed particle method for different

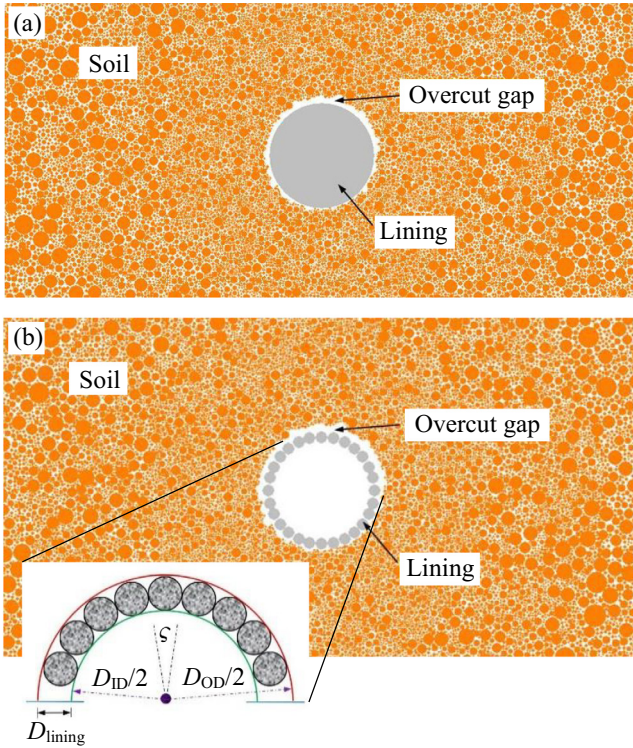


Fig. 14. Schematics of lining model: (a) using a single big particle, and (b) using a layer of small particles.

phases of driving in Fig. 15, along with the field measurements. Calculations are conducted for three types of interface properties, including sandy soils alone, slurry alone, and the sand-slurry mixture (defined by mass ratio of  $m_{\text{sand}}:m_{\text{slurry}}$ ). Without implementation of slurry, one can expect that the friction force at the soil-pipe interface becomes higher, which represents an upper bound of frictional resistance. If the slurry can float the pipe (no direct soil-pipe contact), a lower bound of friction resistance can be derived. For the soil-slurry mixture case, the pipe has partial contact with the sandy soil, but the slurry lubricants can reduce the friction resistance. The measured jacking force falls within the calculated values between the upper bound with sandy soils alone and the case with the sand-slurry mixture.

## 5 Conclusions

Pipe jacking is a trenchless technology to install underground pipelines with minimum disturbance to the ground surface. Pipe segments are jacked through congested urban areas or river crossings between two working shafts. At present, the estimation of the jacking force is often conducted by empirical methods. This use of empirical methods could lead to unnecessary overdesign of the jacking force, which increases the overall costs for a pipe jacking project significantly. In this investigation, a particle method is proposed for the calculation of normal forces around the pipe circumference. A set of microparameters is calibrated

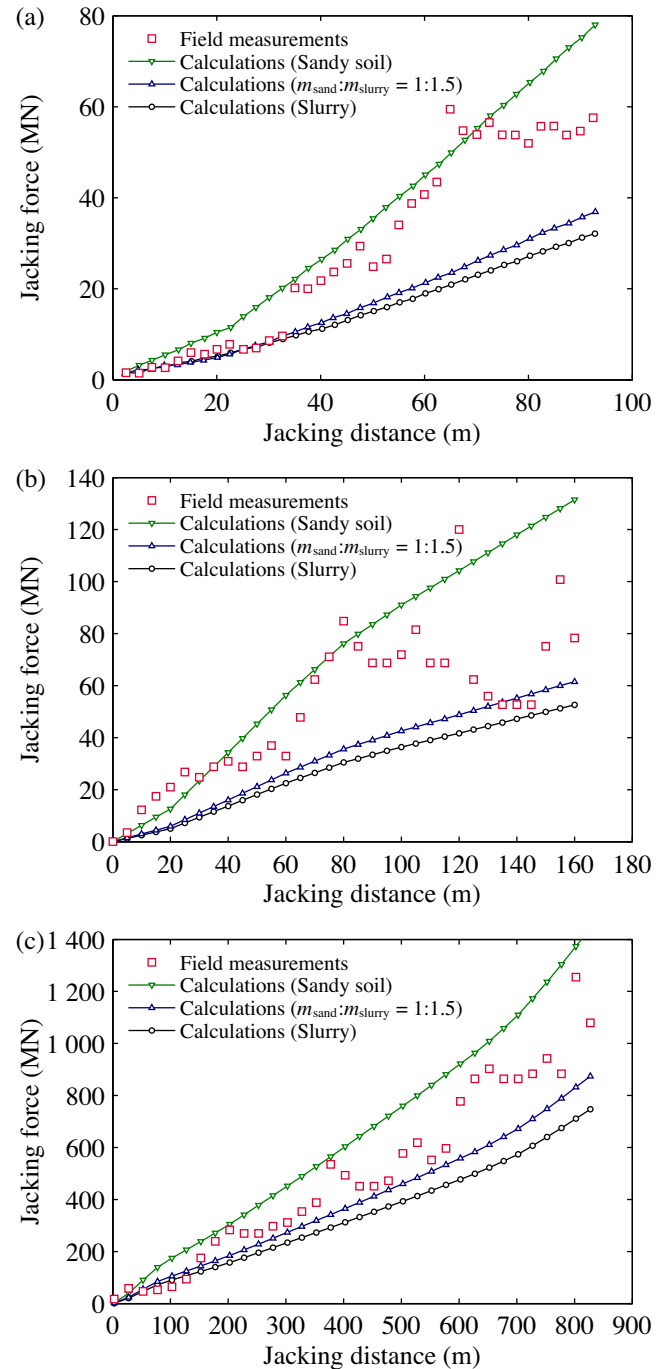


Fig. 15. Comparison between measured and calculated jacking force: (a) hand shield jacking from #2 shaft to #3 shaft, (b) earth pressure balance (EPB) jacking from #3 shaft to #4 shaft, and (c) slurry shield (SS) jacking from #5 shaft to #4 shaft.

to reproduce the macroscale material behavior by comparing numerical calculations under the biaxial conditions with experimental measurements in consolidated drained triaxial compression tests. The normal forces can be multiplied by the interface friction coefficient to determine the frictional resistance mobilized at the soil-pipe interface. The earth pressure acting on the shield face is estimated by the authors based on a modified Protodyakonov's arch

model. Hence, the jacking force can be determined by summing the frictional resistance and earth pressure acting on the shield face. In the end, an illustrative field case of pipe jacking using three different types of jacking machines in Shenyang is presented, for which the calculated jacking forces using the proposed particle method are found to be comparable to the jacking forces measured in the field.

### Conflict of interest

The authors declare that they have no known competing financial interests or personal relationships that could have appeared to influence the work reported in this paper.

### References

- Barla, M., & Camusso, M. (2013). A method to design microtunnelling installations in randomly cemented Torino alluvial soil. *Tunnelling and Underground Space Technology*, 33, 73–81.
- Barla, M., Camusso, M., & Aiassa, S. (2006). Analysis of jacking forces during microtunnelling in limestone. *Tunnelling and Underground Space Technology*, 21(6), 668–683.
- Broere, W., Faassen, T. F., Arends, G., & van Tol, A. F. (2007). Modelling the boring of curves in (very) soft soils during microtunnelling. *Tunnelling and Underground Space Technology*, 22(5), 600–609.
- Camusso, M., & Barla, M. (2009). Microparameters calibration for loose and cemented soil when using particle methods. *International Journal of Geomechanics*, 9(5), 217–229.
- Chapman, D. N., & Ichioka, Y. (1999). Prediction of jacking forces for microtunnelling operations. *Tunnelling and Underground Space Technology*, 14(Supplement 1), 31–41.
- Cheng, W. C., Ni, J. C., Shen, J. S. L., & Huang, H. W. (2017). Investigation into factors affecting jacking force: a case study. *Proceedings of the Institution of Civil Engineers-Geotechnical Engineering*, 170(4), 322–334.
- Cui, Q. L., Xu, Y. S., Shen, S. L., Yin, Z. Y., & Horpibulsuk, S. (2015). Field performance of concrete pipes during jacking in cemented sandy silt. *Tunnelling and Underground Space Technology*, 49, 336–344.
- Huang, X., & Zhang, Z. (2012). Stress arch bunch and its formation mechanism in blocky stratified rock masses. *Journal of Rock Mechanics and Geotechnical Engineering*, 4(1), 19–27.
- Ji, X. (2017). Estimation of jacking force during jacking pipes in Shenyang sandy stratum Ph.D. thesis. Shenyang, China: Northeastern University.
- Ji, X., Ni, P., Barla, M., Zhao, W., & Mei, G. (2018). Earth pressure on shield excavation face for pipe jacking considering arching effect. *Tunnelling and Underground Space Technology*, 72, 17–27.
- Ji, X., Zhao, W., Jia, P., Qiao, L., Barla, M., Ni, P., & Wang, L. (2017). Pipe jacking in sandy soil under a river in Shenyang, China. *Indian Geotechnical Journal*, 47(3), 246–260.
- Ji, X., Zhao, W., Ni, P., Barla, M., Han, J., Jia, P., ... Zhang, C. (2019). A method to estimate the jacking force for pipe jacking in sandy soils. *Tunnelling and Underground Space Technology*, in press.
- Jiang, M., & Yin, Z. Y. (2012). Analysis of stress redistribution in soil and earth pressure on tunnel lining using the discrete element method. *Tunnelling and Underground Space Technology*, 32, 251–259.
- Jiang, M., & Yin, Z. Y. (2014). Influence of soil conditioning on ground deformation during longitudinal tunneling. *Comptes Rendus Mécanique*, 342(3), 189–197.
- Li, Y., Emeriault, F., Kastner, R., & Zhang, Z. X. (2009). Stability analysis of large slurry shield-driven tunnel in soft clay. *Tunnelling and Underground Space Technology*, 24, 472–481.
- Liu, Y. J., Li, G., Yin, Z. Y., Dano, C., Hicher, P. Y., Xia, X. H., & Wang, J. H. (2014). Influence of grading on the undrained behavior of granular materials. *Comptes Rendus Mécanique*, 342(2), 85–95.
- Milligan, G. W. E., & Norris, P. (1999). Pipe-soil interaction during pipe jacking. *Proceedings of the Institution of Civil Engineers – Geotechnical Engineering*, 137(1), 27–44.
- Najafi, M. (2005). Pipe jacking and utility tunneling. *Trenchless technology: Pipeline and utility design, construction, and renewal*. McGraw Hill Professional, Access Engineering.
- Namli, M., & Guler, E. (2017). Effect of bentonite slurry pressure on interface friction of pipe jacking. *Journal of Pipeline Systems Engineering and Practice*, 8(2), 04016016.
- Ni, P. (2016). *Nonlinear soil-structure interaction for buried pressure pipes under differential ground motion* Ph.D. thesis. Kingston, ON, Canada: Queen's University.
- Ni, P., Mei, G., Zhao, Y., & Chen, H. (2018a). Plane strain evaluation of stress paths for supported excavations under lateral loading and unloading. *Soils and Foundations*, 58(1), 146–159.
- Ni, P., Moore, I. D., & Take, W. A. (2018b). Numerical modeling of normal fault-pipeline interaction and comparison with centrifuge tests. *Soil Dynamics and Earthquake Engineering*, 105, 127–138.
- Ni, P., Qin, X., & Yi, Y. (2018c). Numerical study of earth pressures on rigid pipes with tire-derived aggregate inclusions. *Geosynthetic International*, 25(5), 494–506.
- Pellet-Beaucour, A. L., & Kastner, R. (2002). Experimental and analytical study of friction forces during microtunneling operations. *Tunnelling and Underground Space Technology*, 17(1), 83–97.
- Reilly, C. C., & Orr, T. L. (2017). Physical modelling of the effect of lubricants in pipe jacking. *Tunnelling and Underground Space Technology*, 63, 44–53.
- Shimada, H., Khazaei, S., & Matsui, K. (2004). Small diameter tunnel excavation method using slurry pipe-jacking. *Geotechnical & Geological Engineering*, 22(2), 161–186.
- Shou, K., Yen, J., & Liu, M. (2010). On the frictional property of lubricants and its impact on jacking force and soil-pipe interaction of pipe-jacking. *Tunnelling and Underground Space Technology*, 25(4), 469–477.
- Shou, K. J., & Jiang, J. M. (2010). A study of jacking force for a curved pipejacking. *Journal of Rock Mechanics and Geotechnical Engineering*, 2(4), 298–304.
- Wang, S., Huang, R., Ni, P., Ranjith, P. G., & Zhang, M. (2013). Fracture behavior of intact rock using acoustic emission: Experimental observation and realistic modeling. *Geotechnical Testing Journal*, 36(6), 903–914.
- Yen, J., & Shou, K. (2015). Numerical simulation for the estimation the jacking force of pipe jacking. *Tunnelling and Underground Space Technology*, 49, 218–229.
- Yin, Z. Y., Hicher, P. Y., Dano, C., & Jin, Y. F. (2017). Modeling mechanical behavior of very coarse granular materials. *Journal of Engineering Mechanics*, 143(1), C4016006.
- Yin, Z. Y., Huang, H. W., & Hicher, P. Y. (2016). Elastoplastic modeling of sand-silt mixtures. *Soils and Foundations*, 56(3), 520–532.
- Yin, Z. Y., Zhao, J., & Hicher, P. Y. (2014). A micromechanics-based model for sand-silt mixtures. *International Journal of Solids and Structures*, 51(6), 1350–1363.
- Zhang, D., Liu, B., & Qin, Y. (2016a). Construction of a large-section long pedestrian underpass using pipe jacking in muddy silty clay: A case study. *Tunnelling and Underground Space Technology*, 60, 151–164.
- Zhang, H., Zhang, P., Zhou, W., Dong, S., & Ma, B. (2016b). A new model to predict soil pressure acting on deep burial jacked pipes. *Tunnelling and Underground Space Technology*, 60, 183–196.
- Zhang, P., Ma, B. S., Zeng, C., Xie, H. M., Li, X., & Wang, D. W. (2016c). Key techniques for the largest curved pipe jacking roof to date: A case study of Gongbei tunnel. *Tunnelling and Underground Space Technology*, 59, 134–145.